

Lattice-resolution contrast from a focused coherent electron probe. Part II

S.D. Findlay^a, L.J. Allen^{a,*}, M.P. Oxley^a, C.J. Rossouw^b

^a School of Physics, University of Melbourne, Parkville, Vic. 3010, Australia

^b CSIRO Manufacturing Science & Technology, Private Bag 33, Clayton South MDC, Vic. 3169, Australia

Received 15 May 2002; received in revised form 17 October 2002

Abstract

In the previous paper, boundary conditions matching the probe to the crystal wave function in scanning transmission electron microscopy were applied by matching the whole wave function across the boundary. It is shown here how that approach relates to previous Bloch wave formulations using (phase-linked) plane wave boundary conditions for wave vectors implied by the range of transverse momentum components in the incident probe. Matching the whole wave function across the boundary, and including a suitably fine mesh in the reciprocal space associated with the crystal to allow matching of transverse momentum components within the probe, leads to a structure matrix \mathcal{A} containing many elements which would normally be excluded for plane wave incidence. For perfect crystals, the \mathcal{A} -matrix may be block diagonalised. This leads to a considerable increase in the computational efficiency of the model and yields important insights into the physics of convergent probes in perfect crystals—reciprocity in coherent imaging and the small aperture limit for coherent and incoherent contrast are considered. The numerical equivalence of the incoherent lattice contrast calculated in this Bloch wave method and the multislice method using mixed dynamic form factors will be demonstrated. Comparison between both these methods and the frozen phonon model, a prevalent multislice method for annular dark field simulation which has the theoretical advantage of handling double channelling, will be made.

© 2002 Elsevier Science B.V. All rights reserved.

Keywords: Scanning transmission electron microscopy; Coherent electron probe; Lattice-resolution contrast; Coherent contrast; Incoherent contrast; Frozen phonon model

1. Introduction

In the previous paper [1], boundary conditions for scanning transmission electron microscopy (STEM) were applied such that the *total* probe wave function was matched to a crystal wave

function which incorporated *all* the transverse momenta in the incident probe, as usually done in the multislice formulation [2–4]. This differs from the prevalent Bloch wave description of STEM contrast [5–10] which constructs the total wave function from a coherent superposition of Bloch states excited from a series of incident plane waves that span the full range of transverse momentum components in the focused probe. This begs the

*Corresponding author. Fax: +61-3-9347-4783.

E-mail address: lja@physics.unimelb.edu.au (L.J. Allen).

question as to how these methods are related. We will demonstrate that the crystal wave functions produced in these seemingly disparate approaches are identical.

For a focused coherent electron probe, the reciprocal lattice mesh associated with the crystal must be adequate not only for a sampling of the structure of the crystal but also for sampling of the transverse momentum components of the probe. This results in a structure matrix \mathcal{A} which contains elements usually excluded for plane wave incidence. This \mathcal{A} -matrix can be of large order, increasing the numerical demands of the eigenvalue problem to be solved considerably. However, as suggested by Rez [11], the \mathcal{A} -matrix may be block diagonalised in the case of perfect crystals.

Block diagonalisation leads to a natural subdivision of the wave function into pieces based on sets of reciprocal lattice vectors differing by what we will refer to as *physical* reciprocal lattice vectors—those having non-zero structure factors. From this reformulation, the method for applying the boundary conditions in the form of continuity of the entire wave function will be shown to be equivalent to alternative Bloch wave formulations in the literature—those of a coherent superposition of phase-linked plane waves [5–10]. The block diagonalisation provides insight into the physics involved in the coupling of the probe to the wave function in the target. It also lends itself to ready proofs of reciprocity for coherent contrast and to a demonstration of the lack of contrast in coherent and incoherent lattice imaging for apertures which do not encompass a physical reciprocal lattice vector. From a computational point of view, the eigenvalue/eigenvector problem and the calculation of incoherent lattice contrast can be handled for the individual block matrices, with substantial gains in computational efficiency.

The formulation of the previous paper [1] allowed the generalisation of previous cross-section expressions for inelastic scattering, incorporating the concept of the mixed dynamic form factor (MDFF), from the case of incident plane waves to the case of any probe. It was shown there to have an equivalent multislice implementation.

While having the distinct advantage of generality, one possible short-coming of the approach based on the MDFF is that it is assumed that the scattered electrons do not undergo further dynamical diffraction, i.e. a single channelling approximation. The expression for incoherent lattice contrast can be generalised to include double channelling [12] but the calculation then scales as N^8 rather than N^4 , where N is the order of the \mathcal{A} -matrix, and hence is numerically demanding. One multislice method which incorporates double channelling but is only applicable to incoherent imaging based on thermal diffuse scattering (TDS), for example annular dark field (ADF) STEM imaging, is known as the frozen phonon (FPh) model [4,13,14]. Calculations will be presented here which compare the FPh approach with both Bloch wave and multislice implementations of the MDFF approach. The results suggest that the differences between these models may be small for moderately large detectors, in agreement with theoretical arguments [6]. As such, the slight gain in accuracy obtained from the FPh model may in many instances be outweighed by the greater computational efficiency of the Bloch wave or multislice MDFF methods.

Perhaps the most significant conclusion arising from the equivalence of the Bloch wave and multislice MDFF methods of STEM image simulation is that one may choose the most suitable approach to any given problem. The relative computational efficiency of the algorithms is briefly discussed.

2. Calculation of the wave function in the Bloch wave method—block diagonalisation

2.1. Notation

Several different vector notations are used in what follows; the distinctions are worth emphasising. Capitalised vectors \mathbf{G} and \mathbf{H} denote what shall be referred to as *physical* reciprocal lattice vectors, those with non-zero structure factors, the set of which we denote by $\{\mathbf{F}\}$. Lower case vectors \mathbf{g} and \mathbf{h} denote the “nearly continuous” set of reciprocal lattice vectors, as required to sample the transverse

momentum components in a STEM probe. We denote the set thereof by $\{\mathbf{f}\}$.

We shall denote by \mathbf{q}_l an element of the set $\{\mathbf{q}\}$ of vectors about $\mathbf{0}$ which, when added to the vectors in the set $\{\mathbf{F}\}$, produces the set $\{\mathbf{f}\}$. The vectors $\{\mathbf{q}\}$ are all taken to be in the first Brillouin zone. The vector \mathbf{q}_1 will always be taken as $\mathbf{0}$. Note that this construction ensures that any vector \mathbf{g} may uniquely be written as $\mathbf{g} = \mathbf{G} + \mathbf{q}_l$.

The set $\{\mathbf{f}\}$ may be equivalently generated by an $m \times m$ supercell. In this case the subscript l will run from 1 to m^2 . It should be noted that the supercell need not be restricted to $m \times m$ in size, in fact it may be computationally convenient to choose an $m \times n$ supercell where $m \neq n$. For simplicity we will restrict much of the following discussion to $m \times m$, the extension to $m \times n$ being straight forward. One should choose m so as to ensure convergence of incoherent lattice contrast calculations. If convergence under plane wave illumination would require an $N \times N$ \mathcal{A} -matrix (i.e. N elements in the set $\{\mathbf{F}\}$), then an overall \mathcal{A} -matrix in the STEM case of size $m^2 N \times m^2 N$ is used. By using all the physical reciprocal lattice vectors of the supercell, a much finer sampling of the reciprocal mesh is achieved than would be the case for the (smaller) conventional unit cell.

Fig. 1 illustrates the generation of the vector set using the $\langle 001 \rangle$ zone axis orientation for a simple cubic structure and a 2×2 supercell. (Note: It is our experience that typically an 8×8 supercell

is required for converged calculations). For ease of illustration only 49 beams are generated in the physical set $\{\mathbf{F}\}$. The additional vectors for the set $\{\mathbf{f}\}$ are included in this case by the addition of the four reciprocal space vectors \mathbf{q}_l shown. Each subset $\{\mathbf{F} + \mathbf{q}_l\}$ is indicated by the use of differently shaded circles.

2.2. Boundary conditions and the wave function in the crystal

For ease of reference, we repeat here the three key expressions given in the previous paper [1] that describe the wave function in the crystal:

$$\Psi(\mathbf{K}, \mathbf{R}, \mathbf{r}_\perp, z) = \sum_i \alpha^i(\mathbf{R}) \psi^i(\mathbf{K}, \mathbf{r}_\perp, z), \quad (1)$$

$$\psi^i(\mathbf{K}, \mathbf{r}_\perp, z) = \exp(2\pi i \lambda^i z) \sum_{\mathbf{g}} C_{\mathbf{g}}^i \exp(2\pi i \mathbf{g} \cdot \mathbf{r}_\perp), \quad (2)$$

$$\alpha^i(\mathbf{R}) = \sum_{\mathbf{g}} C_{\mathbf{g}}^{i*} \exp(-2\pi i \mathbf{g} \cdot \mathbf{R}) T(\mathbf{g}). \quad (3)$$

An overall phase factor $\exp(2\pi i K z)$, K the wave number corrected for refraction, is omitted in Eq. (2) for simplicity. The $C_{\mathbf{g}}^i$, with “nearly continuous” \mathbf{g} , are Fourier components of the Bloch state i .

Initially it may seem at odds with the Bloch Theorem to be using a mesh finer than the physical reciprocal lattice for the Fourier representation of the crystal potential. However, while it is the physical reciprocal lattice that determines the crystal repeat distance, the incident probe no longer has the translational symmetry of the plane wave case. The wave function in the crystal is *not* the same in adjacent cells up to a phase (the Bloch Theorem), as this does not take the boundary conditions into account. Rather, the intensity of the wave function should, loosely speaking, decrease with increasing distance from the probe position defined by the vector \mathbf{R} . It is the use of Fourier series to represent this non-periodic physical situation that necessitates the use of supercells. The periodic nature of the Fourier series representation means that the supercell is a periodic feature. The probe is effectively positioned at the equivalent position $\mathbf{R} + \mathbf{R}_z$ in each supercell, where \mathbf{R}_z is a vector describing the

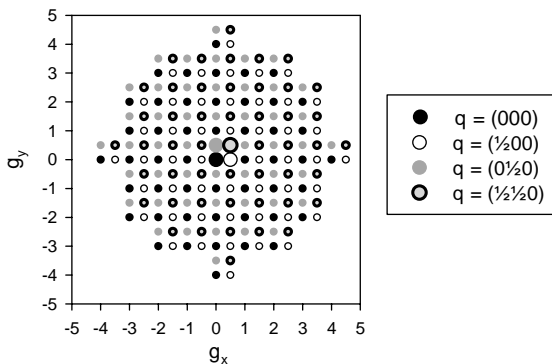


Fig. 1. The vector set $\{\mathbf{f}\}$ generated using a 2×2 supercell (or equivalently the four \mathbf{q} vectors shown and the vector set $\{\mathbf{F}\}$) as described in the text.

repeat distance of the supercell. To ensure that two “probes” located at \mathbf{R} and $\mathbf{R} + \mathbf{R}_\alpha$ do not interact, a sufficiently large supercell must be used. For the cases studied here, an 8×8 supercell is sufficient to ensure converged calculations. This

In using the matrix notation to succinctly express a set of linear equations, there is much freedom to choose the ordering of the rows and columns of the \mathcal{A} -matrix. Allen et al. [16,17] choose the ordering

$$\mathcal{A} = \begin{pmatrix} \vdots & \vdots & \vdots & \vdots & \vdots & \vdots & \vdots \\ \cdots & -(\mathbf{k}_t + \mathbf{h})^2 + iU'_0 & W_{\mathbf{h}-\mathbf{g}} & W_{\mathbf{h}} & W_{\mathbf{h}+\mathbf{g}} & W_{2\mathbf{h}} & \cdots \\ \cdots & W_{\mathbf{g}-\mathbf{h}} & -(\mathbf{k}_t + \mathbf{g})^2 + iU'_0 & W_{\mathbf{g}} & W_{2\mathbf{g}} & W_{\mathbf{g}+\mathbf{h}} & \cdots \\ \cdots & W_{-\mathbf{h}} & W_{-\mathbf{g}} & -\mathbf{k}_t^2 + iU'_0 & W_{\mathbf{g}} & W_{\mathbf{h}} & \cdots \\ \cdots & W_{-\mathbf{g}-\mathbf{h}} & W_{-2\mathbf{g}} & W_{-\mathbf{g}} & -(\mathbf{k}_t - \mathbf{g})^2 + iU'_0 & W_{-\mathbf{g}+\mathbf{h}} & \cdots \\ \cdots & W_{-2\mathbf{h}} & W_{-\mathbf{h}-\mathbf{g}} & W_{-\mathbf{h}} & W_{-\mathbf{h}+\mathbf{g}} & -(\mathbf{k}_t - \mathbf{h})^2 + iU'_0 & \cdots \\ \vdots & \vdots & \vdots & \vdots & \vdots & \vdots & \vdots \end{pmatrix}, \quad (6)$$

will vary depending on the model case under consideration.

2.3. Block diagonalisation

The rationale behind applying the boundary conditions in the form of continuity of the whole wave function across the entrance surface of the crystal has been described in the previous paper [1], and the resultant form of the wave function in the crystal is given above. The presence of many zero elements in the \mathcal{A} -matrix leads to further simplifications of both the description of the wave function within the crystal and the calculation of incoherent lattice contrast.

The Bethe equations [15], including absorption, have the form

$$[K^2 - (\mathbf{k}^i + \mathbf{g})^2 + iU'_0]C_{\mathbf{g}}^i + \sum_{\mathbf{h}(\neq \mathbf{g})} W_{\mathbf{g}-\mathbf{h}} C_{\mathbf{h}}^i = 0, \quad (4)$$

where $W_{\mathbf{g}-\mathbf{h}} = U_{\mathbf{g}-\mathbf{h}} + iU'_{\mathbf{g}-\mathbf{h}}$, and $U_{\mathbf{g}-\mathbf{h}}$ and $U'_{\mathbf{g}-\mathbf{h}}$ denote the coefficients of the elastic and the absorptive potential. Following Allen et al. [16], and the references therein, this may be cast into the matrix form

$$\mathcal{A}\mathcal{C} = 2K\mathcal{C}[\lambda^i]_{\mathbf{D}}, \quad (5)$$

where \mathcal{C} is the matrix of eigenvectors $C_{\mathbf{g}}^i$ and $[\lambda^i]_{\mathbf{D}}$ is the matrix containing the eigenvalues, the subscript \mathbf{D} indicating that it is diagonal in form.

because it makes certain symmetry relations more evident. We will consider the specific case where the tangential component of the incident wave vector $\mathbf{k}_t = \mathbf{0}$ (the exact zone axis orientation). Hence the diagonal elements have the form $-\mathbf{g}^2 + iU'_0$ and are in general non-zero. However, the off-diagonal elements $W_{\mathbf{g}-\mathbf{h}}$ are non-zero only if the vector difference $\mathbf{g} - \mathbf{h}$ is a physical reciprocal lattice vector, i.e.

$$W_{\mathbf{g}-\mathbf{h}} \neq 0 \quad \text{if and only if } \mathbf{g} - \mathbf{h} \in \{\mathbf{F}\}. \quad (7)$$

Remembering that we may uniquely express $\mathbf{g} = \mathbf{G} + \mathbf{q}_l$ and $\mathbf{h} = \mathbf{H} + \mathbf{q}_m$, where the subscripts l and m describe elements of the set $\{\mathbf{q}\}$, then the off-diagonal elements of the \mathcal{A} -matrix may be rewritten as

$$W_{\mathbf{g}-\mathbf{h}} = W_{\mathbf{G}-\mathbf{H}}\delta_{l,m}. \quad (8)$$

Note that, with supercells constructed as described above, this simplification requires that the crystal be periodic. For imperfect crystals this identity does not hold and hence neither do any of the consequences that follow from it.

In the periodic case, the resultant \mathcal{A} -matrix may be reordered in such a way that it is block diagonal (as suggested by Rez [11]) since the elements at the intersection of different groups, described by the subscripts l and m , are all zero. The matrix

equation becomes

$$\begin{aligned}
 & \begin{pmatrix} [\mathcal{A}(\mathbf{q}_1)] & [\mathbf{0}] & \cdots & \cdots & [\mathbf{0}] \\ [\mathbf{0}] & [\mathcal{A}(\mathbf{q}_2)] & \cdots & \cdots & [\mathbf{0}] \\ \cdots & \cdots & \ddots & \cdots & \cdots \\ \cdots & \cdots & \cdots & \ddots & \cdots \\ \cdots & \cdots & \cdots & \cdots & [\mathcal{A}(\mathbf{q}_n)] \end{pmatrix} \\
 & \times \begin{pmatrix} [\mathcal{C}(\mathbf{q}_1)] & [\mathbf{0}] & \cdots & \cdots & [\mathbf{0}] \\ [\mathbf{0}] & [\mathcal{C}(\mathbf{q}_2)] & \cdots & \cdots & [\mathbf{0}] \\ \cdots & \cdots & \ddots & \cdots & \cdots \\ \cdots & \cdots & \cdots & \ddots & \cdots \\ \cdots & \cdots & \cdots & \cdots & [\mathcal{C}(\mathbf{q}_n)] \end{pmatrix} \\
 & = 2K \begin{pmatrix} [\mathcal{C}(\mathbf{q}_1)] & [\mathbf{0}] & \cdots & \cdots & [\mathbf{0}] \\ [\mathbf{0}] & [\mathcal{C}(\mathbf{q}_2)] & \cdots & \cdots & [\mathbf{0}] \\ \cdots & \cdots & \ddots & \cdots & \cdots \\ \cdots & \cdots & \cdots & \ddots & \cdots \\ \cdots & \cdots & \cdots & \cdots & [\mathcal{C}(\mathbf{q}_n)] \end{pmatrix} \\
 & \times \begin{pmatrix} [\lambda(\mathbf{q}_1)]_{\text{D}} & [\mathbf{0}] & \cdots & \cdots & [\mathbf{0}] \\ [\mathbf{0}] & [\lambda(\mathbf{q}_2)]_{\text{D}} & \cdots & \cdots & [\mathbf{0}] \\ \cdots & \cdots & \ddots & \cdots & \cdots \\ \cdots & \cdots & \cdots & \ddots & \cdots \\ \cdots & \cdots & \cdots & \cdots & [\lambda(\mathbf{q}_n)]_{\text{D}} \end{pmatrix}, \quad (9)
 \end{aligned}$$

where each of the m^2 sub-matrices is $N \times N$. The horizontal dots “...” indicate the presence of a matrix of zeros. The diagonal dots “...” indicate the presence of an $[\mathcal{A}(\mathbf{q}_l)]$, $[\mathcal{C}(\mathbf{q}_l)]$ or $[\lambda(\mathbf{q}_l)]_{\text{D}}$ sub-matrix on the diagonal associated with the vector \mathbf{q}_l . The sub-matrices $\mathcal{A}(\mathbf{q}_l)$ (dropping the square brackets for notational convenience) contain the \mathcal{A} -matrix elements with the basis vectors $\{\mathbf{F}\}$ shifted by \mathbf{q}_l . Similarly the sub-matrices $\mathcal{C}(\mathbf{q}_l)$ contain elements of the form $C_{\mathbf{G}}^{l,k} \equiv C_{\mathbf{G}}^k(\mathbf{q}_l)$ where the index k labels the columns of each $N \times N$ sub-matrix. We may now solve the eigenvalue equation by solving the m^2 individual eigenvalue problems

$$\mathcal{A}(\mathbf{q}_l)\mathcal{C}(\mathbf{q}_l) = 2K\mathcal{C}(\mathbf{q}_l)[\lambda^k(\mathbf{q}_l)]_{\text{D}}. \quad (10)$$

The block diagonal form of the \mathcal{C} -matrix in Eq. (9) is due to the existence of unique solutions for the set of eigenvalue equations given in Eq. (10) above. The superscript on the eigenvalues λ^k has been changed to emphasise the fact

that k now labels the N columns within the sub-matrix specified by the label l . Note that the sub-matrix $\mathcal{A}(\mathbf{q}_l)$ is equivalent to that describing plane wave incidence with tangential component $\mathbf{k}_t = \mathbf{q}_l$.

With the reordering used in Eq. (9) we now replace the index i in Eq. (5), which implicitly labels the columns of the complete \mathcal{C} -matrix, with the indices l , describing each sub-matrix $\mathcal{C}(\mathbf{q}_l)$, and k , which denotes the columns of each sub-matrix. Rewriting the equations for the total wave function given by Eq. (1) in terms of summations over l and k

$$\Psi(\mathbf{K}, \mathbf{R}, \mathbf{r}_{\perp}, z) = \sum_{l=1}^{m^2} \sum_{k=1}^N \alpha^{l,k}(\mathbf{R}) \psi^{l,k}(\mathbf{K}, \mathbf{r}_{\perp}, z), \quad (11)$$

where the Bloch states given by Eq. (2) are now

$$\begin{aligned}
 \psi^{l,k}(\mathbf{K}, \mathbf{r}_{\perp}, z) \\
 = \exp(2\pi i \lambda^{l,k} z) \sum_{\mathbf{g}} C_{\mathbf{g}}^{l,k} \exp(2\pi i \mathbf{g} \cdot \mathbf{r}_{\perp}) \quad (12)
 \end{aligned}$$

and the excitation amplitudes given by Eq. (3) become

$$\alpha^{l,k}(\mathbf{R}) = \sum_{\mathbf{g}} C_{\mathbf{g}}^{l,k*} \exp(-2\pi i \mathbf{g} \cdot \mathbf{R}) T(\mathbf{g}). \quad (13)$$

From the block diagonal form in Eq. (9) it immediately follows that $C_{\mathbf{g}}^{l,k} = 0$ for any reciprocal lattice vector $\mathbf{g} \neq \mathbf{G} + \mathbf{q}_l$ [i.e. those elements not contained in the sub-matrix $\mathcal{C}(\mathbf{q}_l)$]. Thus the sums over \mathbf{g} and \mathbf{h} reduce to sums over \mathbf{G} and \mathbf{H} , giving

$$\begin{aligned}
 \psi^{l,k}(\mathbf{K}, \mathbf{r}_{\perp}, z) = \exp(2\pi i \lambda^{l,k} z) \sum_{\mathbf{G}} C_{\mathbf{G}+\mathbf{q}_l}^{l,k} \\
 \times \exp[2\pi i (\mathbf{G} + \mathbf{q}_l) \cdot \mathbf{r}_{\perp}] \quad (14)
 \end{aligned}$$

and

$$\begin{aligned}
 \alpha^{l,k}(\mathbf{R}) = \sum_{\mathbf{G}} C_{\mathbf{G}+\mathbf{q}_l}^{l,k*} \exp[-2\pi i (\mathbf{G} + \mathbf{q}_l) \cdot \mathbf{R}] \\
 \times T(\mathbf{G} + \mathbf{q}_l). \quad (15)
 \end{aligned}$$

We now use the fact that sub-matrix $\mathcal{A}(\mathbf{q}_l)$ is equivalent to that describing plane wave incidence with tangential component $\mathbf{k}_t = \mathbf{q}_l$. From Eq. (10) it is clear that the sub-matrices $\mathcal{C}(\mathbf{q}_l)$ and $\lambda(\mathbf{q}_l)$ must also contain the eigenvectors and eigenvalues describing plane wave incidence for $\mathbf{k}_t = \mathbf{q}_l$. We

may therefore write

$$\begin{aligned} \psi^{l,k}(\mathbf{K}, \mathbf{r}_\perp, z) &= \exp[2\pi i \lambda^k(\mathbf{q}_l) z] \\ &\times \sum_{\mathbf{G}} C_{\mathbf{G}}^k(\mathbf{q}_l) \exp[2\pi i (\mathbf{G} + \mathbf{q}_l) \cdot \mathbf{r}_\perp] \end{aligned} \quad (16)$$

and

$$\begin{aligned} \alpha^{l,k}(\mathbf{R}) &= \sum_{\mathbf{G}} C_{\mathbf{G}}^{k*}(\mathbf{q}_l) \exp[-2\pi i (\mathbf{G} + \mathbf{q}_l) \cdot \mathbf{R}] \\ &\times T(\mathbf{G} + \mathbf{q}_l). \end{aligned} \quad (17)$$

The total wave function given by Eq. (9) is hence a sum over m^2 independent “wave functions”, each associated with a plane wave incidence, with the tangential component of the plane wave being $\mathbf{k}_t = \mathbf{q}_l$. These wave functions do *not* interact with one another. Thus, while the probe contains a continuum of transverse momentum components, inside the crystal these components only interact with others differing in value by physical reciprocal lattice vectors \mathbf{G} .

In the previous paper [1] we discussed Bloch states and Bloch wave amplitudes for normal plane wave incidence ($\mathbf{k}_t = \mathbf{0}$) and noted that the first five Bloch states accounted for over 99% of the incident intensity for plane wave incidence. The block diagonal form of the eigenvalue problem indicates there are likely to be $m^2 - 1$ other such sub-sets of significant Bloch wave amplitudes, which would not normally be excited for plane wave incidence.

Consider a tightly bound s-type state of index k with a concomitantly flat dispersion surface. Fourier coefficients $C_{\mathbf{G}}^k(\mathbf{q}_l)$ of the eigenvector solutions in Eq. (16) may then be considered (to a good approximation) to be independent of \mathbf{q}_l . The eigenvector associated with an s-type state for a primitive unit cell [derived from the sub-matrix $\mathcal{A}(\mathbf{q}_1)$, where $\mathbf{q}_1 = \mathbf{0}$, in the top left-hand corner of the block diagonalised solution of Eq. (9)] may be distributed over the supercell by a simple tiling of these bonding states. This may be used to construct further combinations of bonding/anti-bonding states across the supercell by inclusion of each of the remaining $m^2 - 1$ phase factors $\exp(2\pi i \mathbf{q}_l \cdot \mathbf{r}_\perp)$ separately for each state in the supercell, where $\mathbf{q}_l \neq \mathbf{0}$.

3. Equivalence of global and phase-linked plane wave boundary conditions

In the previous work using a Bloch wave framework [5–10,18,19], the boundary conditions are applied in a conceptually different form. Those works treat each component with differing transverse momentum in the probe as if it were a plane wave in isolation, match the boundary conditions accordingly, and *then* perform the coherent sum to obtain the total wave function. This is predicated on the notion of superposition, whereby the response to the whole incident wave field is the sum of the responses to individual components. Thus the incident probe is treated not so much as a distorted wavefront, but rather as a coherent superposition of phase-linked plane waves.

The boundary conditions have not previously been applied in the Bloch wave formalism in the manner described in the previous paper [1]. We will now show that the phase-linked plane wave approach is formally equivalent to that described here, which has a conceptually different foundation. As such, both techniques offer different insights into the physics of the problem. It is worth noting that in calculation of convergent beam electron diffraction (CBED) patterns, multislice methods have been applied with both approaches to the boundary conditions [20].

Eq. (5) in the paper of Nellist and Pennycook [6] expresses the total wave function as obtained in the phase-linked plane wave boundary conditions approach. That equation, re-drafted for consistency with the notation and sign conventions used here, reads

$$\begin{aligned} \Phi(\mathbf{K}, \mathbf{R}, \mathbf{r}_\perp, z) &= \int \sum_{k=1}^N \beta^k(\mathbf{R}, \mathbf{p}) \\ &\times \phi^k(\mathbf{K}, \mathbf{p}, \mathbf{r}_\perp, z) d\mathbf{p}, \end{aligned} \quad (18)$$

where β^k is the excitation amplitude of Bloch wave ϕ^k . Note that the superscript k is used here, denoting that the sum is over the N columns of the plane wave \mathcal{C} -matrices. Bloch waves are resolved for each transverse component \mathbf{p} of the focused

probe

$$\phi^k(\mathbf{K}, \mathbf{p}, \mathbf{r}_\perp, z) = \exp[2\pi i \lambda^k(\mathbf{p})z] \sum_{\mathbf{G}} C_{\mathbf{G}}^k(\mathbf{p}) \times \exp[2\pi i(\mathbf{p} + \mathbf{G}) \cdot \mathbf{r}_\perp], \quad (19)$$

where again a factor of $\exp(2\pi i Kz)$ has been omitted. The excitation amplitude is

$$\beta^k(\mathbf{R}, \mathbf{p}) = C_0^{k*}(\mathbf{p}) \exp(-2\pi i \mathbf{p} \cdot \mathbf{R}) T(\mathbf{p}). \quad (20)$$

We will now demonstrate that this formalism is equivalent to that afforded by the block diagonalisation, and therefore to that presented in the previous paper [1].

Replacing the integral in the total wave function Eq. (18) by a sum over “nearly continuous” \mathbf{p} , breaking it up into a sum over physical vectors \mathbf{H} and a sum over l labelling the vectors of the set $\{\mathbf{q}\}$ gives

$$\Phi(\mathbf{K}, \mathbf{R}, \mathbf{r}_\perp, z) = \sum_{l=1}^{m^2} \sum_{\mathbf{H}} \sum_{k=1}^N \beta^k(\mathbf{R}, \mathbf{H} + \mathbf{q}_l) \times \phi^k(\mathbf{K}, \mathbf{H} + \mathbf{q}_l, \mathbf{r}_\perp, z), \quad (21)$$

where

$$\begin{aligned} \phi^k(\mathbf{K}, \mathbf{H} + \mathbf{q}_l, \mathbf{r}_\perp, z) &= \exp[2\pi i \lambda^k(\mathbf{H} + \mathbf{q}_l)z] \sum_{\mathbf{G}} C_{\mathbf{G}}^k(\mathbf{H} + \mathbf{q}_l) \\ &\times \exp[2\pi i(\mathbf{G} + \mathbf{H} + \mathbf{q}_l) \cdot \mathbf{r}_\perp]. \end{aligned} \quad (22)$$

Before proceeding, recall that in the plane wave case the eigenvalues and eigenvector elements obey the following periodicity relations [21]:

$$\begin{aligned} C_{\mathbf{G}-\mathbf{H}}^k(\mathbf{K} + \mathbf{H}) &= C_{\mathbf{G}}^k(\mathbf{K}), \\ \lambda^k(\mathbf{K} + \mathbf{H}) &= \lambda^k(\mathbf{K}). \end{aligned} \quad (23)$$

Substituting these periodicity relationships into Eq. (22), we may bring the vector \mathbf{H} out of the argument and into the subscript. This results in an expression in the sum over \mathbf{G} of terms depending on $\mathbf{G} + \mathbf{H}$. This is a basis shift, and we may re-label the sum as follows.

$$\begin{aligned} \phi^k(\mathbf{K}, \mathbf{H} + \mathbf{q}_l, \mathbf{r}_\perp, z) &= \exp[2\pi i \lambda^k(\mathbf{q}_l)z] \\ &\times \sum_{\mathbf{G}} C_{\mathbf{G}+\mathbf{H}}^k(\mathbf{q}_l) \exp[2\pi i(\mathbf{G} + \mathbf{H} + \mathbf{q}_l) \cdot \mathbf{r}_\perp] \\ &= \exp[2\pi i \lambda^k(\mathbf{q}_l)z] \\ &\times \sum_{\mathbf{G}} C_{\mathbf{G}}^k(\mathbf{q}_l) \exp[2\pi i(\mathbf{G} + \mathbf{q}_l) \cdot \mathbf{r}_\perp]. \end{aligned} \quad (24)$$

The result is that $\phi^k(\mathbf{K}, \mathbf{H} + \mathbf{q}_l, \mathbf{r}_\perp, z) \equiv \phi^k(\mathbf{K}, \mathbf{q}_l, \mathbf{r}_\perp, z)$, containing no dependence on the vector \mathbf{H} . Note that the above Bloch wave expression is identical to the Bloch wave expression of the block diagonal form, Eq. (16), so $\phi^k(\mathbf{K}, \mathbf{q}_l, \mathbf{r}_\perp, z) \equiv \psi^{l,k}(\mathbf{K}, \mathbf{r}_\perp, z)$.

Because there is no \mathbf{H} dependence in ϕ^k , the sum over \mathbf{H} in the total wave function, Eq. (21), may be grouped with the excitation amplitudes β^k . But

$$\begin{aligned} \sum_{\mathbf{H}} \beta^k(\mathbf{R}, \mathbf{H} + \mathbf{q}_l) &= \sum_{\mathbf{H}} C_0^{k*}(\mathbf{H} + \mathbf{q}_l) \exp[-2\pi i(\mathbf{H} + \mathbf{q}_l) \cdot \mathbf{R}] \\ &\times T(\mathbf{H} + \mathbf{q}_l) \\ &= \sum_{\mathbf{H}} C_{\mathbf{H}}^{k*}(\mathbf{q}_l) \exp[-2\pi i(\mathbf{H} + \mathbf{q}_l) \cdot \mathbf{R}] \\ &\times T(\mathbf{H} + \mathbf{q}_l), \end{aligned} \quad (25)$$

where again we have made use of the periodicity relations. Now note that the above equation is identical to the block diagonal expression for the excitation amplitudes, Eq. (17). So $\sum_{\mathbf{H}} \beta^k(\mathbf{R}, \mathbf{H} + \mathbf{q}_l) \equiv \alpha^{l,k}(\mathbf{R})$. Thus Eqs. (21), (24) and (25) describing the wave function are identical to Eqs. (11), (16) and (17). The wave functions in the two formulations are equivalent.

In obtaining the block diagonal form from the formulation of the previous paper [1], it was shown that no connection exists between wave functions described by plane waves with wave vectors which do not differ by a physical reciprocal lattice vector, although it initially seemed implied by that model. In working the phase-linked plane wave approach towards an equivalent form it was shown, by subsuming the sum over \mathbf{H} into the terms β^k and ϕ^k , that a meaningful physical connection exists between incident plane waves with wave vectors

differing by a physical reciprocal lattice vector, although it initially seemed that this was not implied by that model. This is the insight gained through the comparison of these models. Thus the useful physical picture and efficient coding method is the half-way point between the two formulations.

4. Reciprocity—coherent imaging

In the previous paper [1] it was emphasised that this Bloch wave formulation for the STEM wave function in no way made use of assumptions of reciprocity. However the result of reciprocity is well established [22–24]; the technique presented must reproduce it. It shall now be shown that the phenomenon of reciprocity follows naturally from this formulation. In this section we will use Ψ to denote reciprocal space wave functions and ψ to denote real space wave functions. Fig. 2 shows schematically the formation of a diffraction pattern in STEM and an image in transmission electron microscopy (TEM).

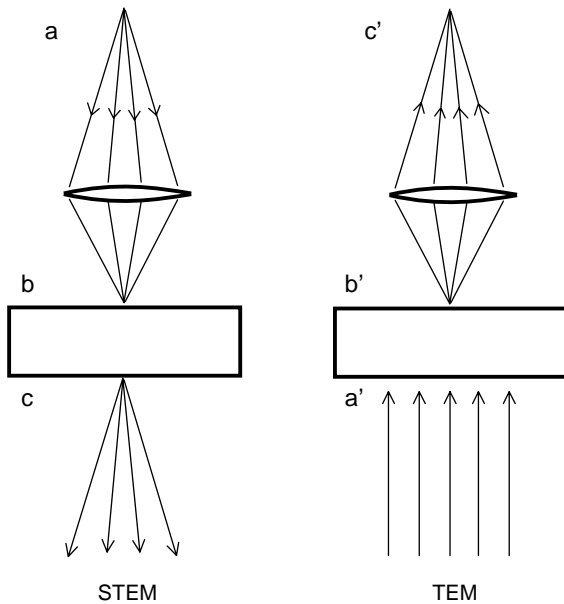


Fig. 2. Schematic of electron diffraction in STEM producing a diffraction image (left) and in TEM to produce an exit surface image (right).

Consider first the STEM case, taking the incident wave to originate from a point source. The reciprocal (Fourier space) representation of the wave function at the source, labelled (a) in Fig. 2, is unity

$$\Psi_a(\mathbf{p}) = 1. \quad (26)$$

Transmission through the lens, in the reciprocal space notation, is obtained by multiplication by the contrast transfer function (CTF) of the lens, denoted $T(\mathbf{p})$. In addition we must introduce the phase factor $\exp(-2\pi i \mathbf{p} \cdot \mathbf{R})$ to account for the position of the centre of the lens with respect to a chosen origin on the crystal surface. The reciprocal space representation of the wave function at (b) is then

$$\Psi_b(\mathbf{p}) = T(\mathbf{p}) \exp(-2\pi i \mathbf{p} \cdot \mathbf{R}). \quad (27)$$

The real space wave function is simply the Fourier transform of this

$$\psi_b(\mathbf{r}) = \sum_{\mathbf{p}} T(\mathbf{p}) \exp(-2\pi i \mathbf{p} \cdot \mathbf{R}) \exp(2\pi i \mathbf{p} \cdot \mathbf{r}). \quad (28)$$

We now introduce the concept of the \mathcal{S} -matrix. The \mathcal{S} -matrix relates the incident and exit surface waves. Specifically, $\mathcal{S}_{\mathbf{g},\mathbf{h}}$ is the transition amplitude for the incident plane wave component labelled \mathbf{h} to be transmitted to the exit plane wave component labelled \mathbf{g} . $\mathcal{S}_{\mathbf{g},\mathbf{h}}$ is given by Allen et al. [16]

$$\mathcal{S}_{\mathbf{g},\mathbf{h}} \equiv \sum_i C_{\mathbf{g}}^i \exp(2\pi i \lambda^i t) C_{\mathbf{h}}^{i*}. \quad (29)$$

Using Eq. (29) and the reciprocal space representation for the entrance surface wave function at (b) given in Eq. (27), the reciprocal space representation for the exit surface wave function is

$$\begin{aligned} \Psi_c(\mathbf{q}) &= \sum_{\mathbf{p}} \mathcal{S}_{\mathbf{q},\mathbf{p}} T(\mathbf{p}) \exp(-2\pi i \mathbf{p} \cdot \mathbf{R}) \\ &= \sum_{\mathbf{p}} \left[\sum_i C_{\mathbf{q}}^i \exp(2\pi i \lambda^i t) C_{\mathbf{p}}^{i*} \right] \\ &\quad \times T(\mathbf{p}) \exp(-2\pi i \mathbf{p} \cdot \mathbf{R}). \end{aligned} \quad (30)$$

The bright field STEM amplitude is simply the zeroth component of the above expression

$$\begin{aligned} A_0^{\text{STEM}} &= \Psi_c(\mathbf{0}) = \sum_{\mathbf{H}} \left[\sum_i C_0^i \exp(2\pi i \lambda^i t) C_{\mathbf{H}}^{i*} \right] \\ &\quad \times T(\mathbf{H}) \exp(-2\pi i \mathbf{H} \cdot \mathbf{R}). \end{aligned} \quad (31)$$

Note that this is Eq. (11) of the previous paper [1] for the diffraction amplitude. There the restriction to the subset of vectors \mathbf{H} associated with the fundamental unit cell was taken as an assumption. Now it is seen to be a direct consequence of the concepts underlying the block diagonalisation.

Now consider the TEM case. The above treatment followed the standard convention that the z -direction is identified with the incident beam direction—down in Fig. 2 for STEM. For the following treatment of TEM we will break that; instead we shall retain the z -direction as down, despite the incident beam direction being up in Fig. 2. Thus here we shall be propagating “backwards”. In order to do so we may be guided by the rationale that the operations performed should, if applied to the STEM case described above, be those which undo the operations performed there.

With this in mind, propagating “backwards” through the crystal is accomplished in a matrix sense by multiplying by \mathcal{S}^{-1} . To do this we must neglect absorption (absorption removes the idealised result of reciprocity, though see Pogany and Turner [25] for a discussion of approximate reciprocity including inelastic scattering). If we neglect absorption, then the \mathcal{S} -matrix is unitary: $\mathcal{S}^{-1} \equiv \mathcal{S}^\dagger$. Careful consideration of the matrices then gives

$$\begin{aligned}\mathcal{S} &= \mathcal{C}[\exp(2\pi i \lambda^i t)]_D \mathcal{C}^\dagger, \\ \mathcal{S}^{-1} &= \mathcal{S}^\dagger = \mathcal{C}[\exp(-2\pi i \lambda^i t)]_D \mathcal{C}^\dagger,\end{aligned}\quad (32)$$

which is also the result obtained by putting $t \rightarrow -t$ in Eq. (29). Examining individual elements

$$\mathcal{S}_{\mathbf{g},\mathbf{h}}^\dagger \equiv \sum_i C_{\mathbf{g}}^i \exp(-2\pi i \lambda^i t) C_{\mathbf{h}}^{i*}. \quad (33)$$

In TEM, as shown in Fig. 2, the incident plane wave at (a') is given by the reciprocal space representation

$$\Psi_{\mathbf{a}'}(\mathbf{p}) = \delta_{\mathbf{p},0}. \quad (34)$$

The reciprocal space representation for the wave function at (b') may then be obtained by interpreting $\mathcal{S}_{\mathbf{g},\mathbf{h}}^\dagger$ as the transition amplitude for incident plane wave labelled \mathbf{h} to the exit plane

wave labelled \mathbf{g} . So

$$\begin{aligned}\Psi_{\mathbf{b}'}(\mathbf{h}) &= \sum_{\mathbf{p}} \mathcal{S}_{\mathbf{h},\mathbf{p}}^\dagger \delta_{\mathbf{p},0} = \mathcal{S}_{\mathbf{h},0}^\dagger, \\ \Psi_{\mathbf{b}'}(\mathbf{H}) &= \sum_i C_{\mathbf{H}}^i \exp(-2\pi i \lambda^i t) C_0^{i*},\end{aligned}\quad (35)$$

where we have changed notation \mathbf{h} to \mathbf{H} to reflect that in the plane wave case the exit surface wave comprises only plane waves related to the incident plane wave by tilts of physical reciprocal lattice vectors.

As in the STEM case, the positioning of the lens means that the reciprocal space representation of the image results from multiplying the reciprocal space wave function at (b') with the complex conjugate of the CTF (corresponding to propagating backwards through the lens)

$$\Psi_{\mathbf{c}'}(\mathbf{H}) = \sum_i C_{\mathbf{H}}^i \exp(-2\pi i \lambda^i t) C_0^{i*} T^*(\mathbf{H}). \quad (36)$$

Finally, the real space wave function in the image plane at (c') is constructed by inverse Fourier transform, giving

$$\begin{aligned}A_{\text{TEM}}(\mathbf{R}) &= \psi_{\mathbf{c}'}(\mathbf{R}) \\ &= \sum_{\mathbf{H}} \left[\sum_i C_{\mathbf{H}}^i \exp(-2\pi i \lambda^i t) C_0^{i*} \right] \\ &\quad \times T^*(\mathbf{H}) \exp(2\pi i \mathbf{H} \cdot \mathbf{R}).\end{aligned}\quad (37)$$

Note that \mathbf{R} has now been used to describe the position in the image. This usage is different to that in the STEM discussion. However this notational subtlety has been tolerated because it aids a comparison between Eqs. (31) and (37). Inspection shows that they are the complex conjugates of one another, in particular they have the same magnitude. The phase is irrelevant, since it has little meaning in the diffraction plane in the STEM case. Thus the reciprocity theorem for the equivalence of TEM and STEM as appearing in the literature [22–24] has been demonstrated from the Bloch wave expression for the wave function.

5. Rapid calculation of incoherent scattering contrast—Bloch wave method

In the previous paper [1], the following expression for the cross section per unit volume for inelastic scattering was presented

$$\sigma(\mathbf{R}, t) = \sum_{i,j} B^{ij}(\mathbf{R}, t) \sum_{\mathbf{g}, \mathbf{h}} C_{\mathbf{g}}^i C_{\mathbf{h}}^{j*} \mu_{\mathbf{h}, \mathbf{g}} + \left[1 - \sum_{i,j} B^{ij}(\mathbf{R}, t) \sum_{\mathbf{g}} C_{\mathbf{g}}^i C_{\mathbf{g}}^{j*} \right] \mu_{0,0}, \quad (38)$$

where

$$B^{ij}(\mathbf{R}, t) = \alpha^i(\mathbf{R}) \alpha^{j*}(\mathbf{R}) \frac{\exp[2\pi i(\lambda^i - \lambda^{j*})t] - 1}{2\pi i(\lambda^i - \lambda^{j*})t}. \quad (39)$$

The first term in Eq. (38) represents the z -integrated dynamical contribution to $\sigma(\mathbf{R}, t)$ after absorption, and the second term accounts for a background contribution from absorbed electrons. Eqs. (38) and (39) provide a framework for calculating the cross section for any incoherent scattering process via the inelastic scattering coefficients $\mu_{\mathbf{h}, \mathbf{g}}$. For TDS this includes incoherent scattering detected by ADF or back-scattered electron (BSE) detectors. For ionisation this includes electron energy loss spectroscopy (EELS) and energy dispersive X-ray (EDX) analysis.

We now recast this expression into matrix form. For clarity we will adopt the following notation. $C_{\mathbf{g}, i} \equiv C_{\mathbf{g}}^i \in \mathcal{C}$, the matrix of eigenvectors. Also we define $B_{i,j} \equiv B^{ij}(\mathbf{R}, t) \in \mathcal{B}$ and $\mu_{\mathbf{h}, \mathbf{g}} \in \mathcal{U}$, where \mathcal{B} and \mathcal{U} are $m^2 N \times m^2 N$ matrices. In this notation the first subscript labels the rows and the second subscript the columns of each matrix. We will also use the superscript T to represent the transpose of these matrices and their related elements. For example $C_{\mathbf{g}, i} = C_{i, \mathbf{g}}^T \in \mathcal{C}^T$.

We first consider the sum occurring in the diffuse contribution to the inelastic cross section.

$$\begin{aligned} \sum_{i,j} B_{i,j} \sum_{\mathbf{g}} C_{\mathbf{g}, i} C_{\mathbf{g}, j}^* &= \sum_{i,j} B_{i,j} \sum_{\mathbf{g}} C_{i, \mathbf{g}}^T C_{\mathbf{g}, j}^* \\ &= \sum_{i,j} B_{i,j} (\mathcal{C}^T \mathcal{C}^*)_{i,j} \\ &= \sum_j \sum_i B_{j,i}^T (\mathcal{C}^T \mathcal{C}^*)_{i,j} \\ &= \sum_j (\mathcal{B}^T \mathcal{C}^T \mathcal{C}^*)_{j,j} \\ &= \text{Tr}(\mathcal{B}^T \mathcal{C}^T \mathcal{C}^*). \end{aligned} \quad (40)$$

Similarly we may write the dynamical contribution as

$$\begin{aligned} \sum_{i,j} B_{i,j} \sum_{\mathbf{h}, \mathbf{g}} C_{\mathbf{h}, j}^* \mu_{\mathbf{h}, \mathbf{g}} &= \sum_{i,j} B_{i,j} \sum_{\mathbf{h}} C_{\mathbf{h}, j}^* \sum_{\mathbf{g}} \mu_{\mathbf{h}, \mathbf{g}} C_{\mathbf{g}, i} \\ &= \sum_{i,j} B_{i,j} \sum_{\mathbf{h}} C_{\mathbf{h}, j}^* (\mathcal{U} \mathcal{C})_{\mathbf{h}, i} \\ &= \sum_{i,j} B_{i,j} \sum_{\mathbf{h}} C_{j, \mathbf{h}}^{*T} (\mathcal{U} \mathcal{C})_{\mathbf{h}, i} \\ &= \sum_i \sum_j B_{i,j} (\mathcal{C}^{*T} \mathcal{U} \mathcal{C})_{j,i} \\ &= \sum_i (\mathcal{B} \mathcal{C}^{*T} \mathcal{U} \mathcal{C})_{i,i} \\ &= \text{Tr}(\mathcal{B} \mathcal{C}^{*T} \mathcal{U} \mathcal{C}). \end{aligned} \quad (41)$$

Hence the inelastic cross section per unit volume may be written

$$\sigma(\mathbf{R}, t) = \text{Tr}(\mathcal{B} \mathcal{C}^{*T} \mathcal{U} \mathcal{C}) + [1 - \text{Tr}(\mathcal{B}^T \mathcal{C}^T \mathcal{C}^*)] \mu_{0,0}. \quad (42)$$

We now make use of the block diagonal nature of the eigenvalue problem. Because the matrices \mathcal{C} and \mathcal{U} are both block diagonal, the matrix products $\mathcal{C}^{*T} \mathcal{U} \mathcal{C}$ and $\mathcal{C}^T \mathcal{C}^*$ occurring in Eq. (9) are also block diagonal. Therefore the calculation of $\text{Tr}(\mathcal{B} \mathcal{C}^{*T} \mathcal{U} \mathcal{C})$ and $\text{Tr}(\mathcal{B}^T \mathcal{C}^T \mathcal{C}^*)$ involves only terms in the matrix \mathcal{B} that correspond to the sub-matrices $\mathcal{C}(\mathbf{q}_l)$ and $\mathcal{U}(\mathbf{q}_l)$ and hence only these terms need be calculated. We shall denote these sub-matrices as $\mathcal{B}(\mathbf{q}_l)$. Eq. (42) can thus be

expressed as a sum of traces for each sub-matrix

$$\begin{aligned} \sigma(\mathbf{R}, t) = & \sum_{l=1}^{m^2} \text{Tr}[\mathcal{B}(\mathbf{q}_l) \mathcal{C}^{*T}(\mathbf{q}_l) \mathcal{U}(\mathbf{q}_l) \mathcal{C}(\mathbf{q}_l)] \\ & + \left\{ 1 - \sum_{l=1}^{m^2} \text{Tr}[\mathcal{B}^T(\mathbf{q}_l) \mathcal{C}^T(\mathbf{q}_l) \right. \\ & \left. \times \mathcal{C}^*(\mathbf{q}_l)] \right\} \mu_{0,0}, \end{aligned} \quad (43)$$

where $\mathcal{C}(\mathbf{q}_l)$ and $\lambda(\mathbf{q}_l)$ [required for the evaluation of $\mathcal{B}(\mathbf{q}_l)$] are calculated using Eq. (10).

Since the numerical solution of an eigenvalue problem goes as the third power of the order of the matrix [26], one may utilise the block diagonal nature of the problem so that in calculating for the wave function, rather than solving the eigenvalue problem for an order $m^2 N$ matrix [which scales as $(m^2 N)^3$], one can solve the eigenvalue problem for m^2 matrices of order N [which scales as $m^2(N^3)$]. Since fully converged calculations require $m \simeq 8$, this gives a reduction of computation time of the order of 10^3 —a considerable gain in the computational efficiency for this model.

In addition, the dynamical term given in Eq. (41) scales as the fourth power of the order of the matrix. Block diagonalisation reduces the problem from scaling as $(m^2 N)^4$ to scaling as $m^2(N^4)$. For $m = 8$ as used above, a reduction in size of the numerical problem of the order of 10^5 is obtained.

The matrix products $\mathcal{C}^{*T}(\mathbf{q}_l) \mathcal{U}(\mathbf{q}_l) \mathcal{C}(\mathbf{q}_l)$ and $\mathcal{C}^T(\mathbf{q}_l) \mathcal{C}^*(\mathbf{q}_l)$ are independent of probe position \mathbf{R} , the \mathbf{R} dependence being confined to the matrix $\mathcal{B}(\mathbf{q}_l)$. This means that they need only be calculated once, and only $\mathcal{B}(\mathbf{q}_l)$ needs be recalculated as a function of position. Equivalently, the summations over \mathbf{g} and \mathbf{h} occurring in Eq. (38) need only be calculated once, with cross sections for subsequent probe positions requiring only summations over i and j .

6. The small aperture limit for incoherent contrast—Bloch wave method

The conceptualisation resulting from the block diagonalisation has been shown to yield a ready

proof of the equivalence between our approach of matching the whole wave function at the incident boundary and the technique for the coherent superposition of phase-linked plane waves. It also led to a simplification of the inelastic cross-section expression for perfect crystals. It can further be shown to lend itself to ready proofs of some well-known properties of STEM images, namely the lack of contrast present in STEM images when the aperture is too narrow to allow transverse momentum components which differ by a physical reciprocal lattice vector [20,27].

The statement is commonly seen that coherent STEM image contrast requires an aperture that encompasses at least two beams with tangential component differing by a physical reciprocal lattice vector [27]. It will now be demonstrated, in the Bloch wave, block diagonal formalism, that this is equally true for the case of incoherent contrast. For completeness, a discussion of the small aperture limit for coherent contrast is given in Appendix A.

Consider an aperture of size less than the magnitude of the smallest (non-forbidden) \mathbf{G} vector which, for normal incidence, will be centred on the origin of reciprocal space. Thus it is assumed that

$$T(\mathbf{H} + \mathbf{q}_l) = \delta_{\mathbf{H},0} T(\mathbf{q}_l). \quad (44)$$

Substituting this into Eq. (17) for the excitation amplitude in the block diagonal formulation

$$\alpha^k(\mathbf{R}) = C_0^{k*}(\mathbf{q}_l) \exp(-2\pi i \mathbf{q}_l \cdot \mathbf{R}) T(\mathbf{q}_l). \quad (45)$$

Thus all the \mathbf{R} dependence is coupled to terms \mathbf{q}_l . But the block diagonal formulation has shown that the contributions from differing \mathbf{q}_l may be added together separately. For any given wave function \mathbf{q}_l , the terms B^{ij} contain \mathbf{R} dependence only through the expression $\alpha^{i'}(\mathbf{R}) \alpha^{j'*}(\mathbf{R})$ which, from the form of Eq. (45) above, is independent of \mathbf{R} . Thus the resultant images contain no contrast at all.

Fig. 3 shows a simulation of ADF incoherent lattice contrast in $\langle 110 \rangle$ ZnS as a function of aperture size. The magnitude of the smallest physical reciprocal lattice vector is 0.32 \AA^{-1} , which is just excluded by an aperture with radius 0.16 \AA^{-1} . We indeed see a steady reduction in

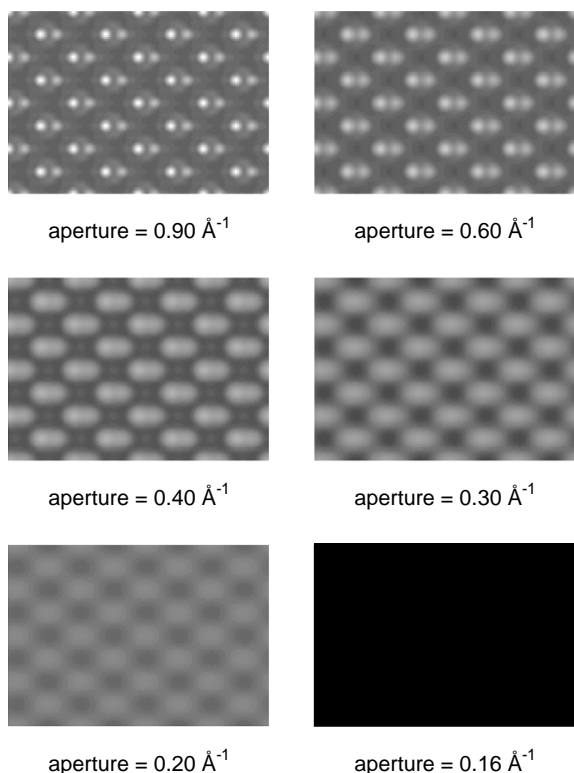


Fig. 3. ADF STEM image contrast for the case of electrons incident along the $\langle 110 \rangle$ zone axis of ZnS, with incident energy of 200 keV, for different aperture sizes. A spherical aberration coefficient C_s of 0.05 mm and the corresponding Scherzer defocus of 129.3 \AA have been assumed. The ADF detector spans $60\text{--}160 \text{ mrad}$. The aperture size of 0.90 \AA^{-1} is the optimal case. The aperture size of 0.16 \AA^{-1} is fractionally too small to encompass reciprocal vectors differing by a full physical reciprocal lattice vector and as such the resulting STEM image has no contrast, as predicted.

contrast as the aperture size is reduced from the optimal aperture of 0.90 \AA^{-1} to an aperture of 0.16 \AA^{-1} , this last giving no contrast.

7. Comparison of the FPh model and the MDFF model for ADF imaging

That multislice methods have been applied using both formulations of the boundary conditions discussed in this paper, see for example Self and O'Keefe [20], suggests that a multislice algorithm

may also be used to calculate STEM images using the MDFF method. Such an algorithm has been presented by Ishizuka [28,29]. A generalisation of this, incorporating a diffuse background term and allowing nonlocal as well as local potentials, was presented in the previous paper [1]. Calculations of incoherent STEM images in the Bloch wave and multislice MDFF models have shown that excellent numerical agreement exists between these algorithms.

However, before we present one such calculation, there is another related comparison of interest. The plane wave theory, of which the Bloch wave model for incoherent lattice-resolution contrast described in the preceding paper is a generalisation, has been used successfully in calculating channelling contrast as a function of rocking beam orientation for TDS into ADF or BSE detectors, as well as for contrast derived from atomic ionisation events and observed by EELS or EDX [30–33]. This gives much confidence in the validity of the method; the generality of the method is another strong point in its favour. One noteworthy approximation made is the assumption of single channelling. Since a multislice MDFF algorithm has been presented, the question naturally arises as to how the results of these calculations compare to the FPh model, a multislice model which, though readily applicable only to ADF simulations, naturally takes double channelling into account. It is interesting and instructive therefore to compare three models for ADF STEM imaging—the Bloch wave MDFF model, the multislice MDFF model and the multislice FPh model.

We begin with a very brief summary of the concepts behind the FPh model, drawing heavily on the discussions by Loane and co-workers [4,13,14].

In the MDFF method we deal with the thermal motion of atoms in an Einstein model using Debye-Waller factors. In that model, the atoms are treated as stationary, but the potential is effectively time-averaged. However it may be reasoned [13] that the interaction time of the incident electrons with any particular atom in the solid is on the order of 10^{-4} vibrational periods of the atom. Therefore, any given electron can be said

to see a static configuration of atomic positions. Note that the motion of the atoms means that not all electrons see this same distribution. Thus another way to build up a physically reasonable picture is to determine the average diffraction pattern for several different thermal configurations of atomic positions. It may be argued [14] that the different electrons see different distributions of atoms which are essentially uncorrelated with one another. As such, the average taken is incoherent—an average over intensities (rather than complex amplitudes). This constitutes a Monte Carlo style integration over phonon configuration space. This is the essence of the FPh model.

The position of atoms in a specimen for a given “run” are formed by displacing each atom a distance based on a Gaussian probability distribution arising from a simple harmonic oscillator model. Loane et al. [13,14] have demonstrated that to get a random sampling of phonon configuration space, rather than calculating a new random slice for each successive “run”, it is sufficient to randomly displace the lattice sites by integer multiples of the lattice translation vectors in either direction.

“A natural consequence of explicitly calculating the scattering from each phonon configuration is the inclusion of multiple elastic and TDS scattering to all orders” [13]. As such, the images display a thermal background showing Kikuchi band structure. In this sense, it may be argued that the FPh model is theoretically more realistic, though there is some reason to expect that for ADF STEM images the integration over the annular detector is such that the difference between these two models on this score should be small [6]. It is this sort of issue that our comparison between the methods will endeavour, in an empirical sense, to address.

In conformity with the previous paper, we will consider the incoherent ADF STEM image resulting from scattering through $\langle 110 \rangle$ ZnS. Because of the computational demands of the FPh model, only line scans will be shown. Fig. 4 shows the projected potential for $\langle 110 \rangle$ ZnS with the line scan denoted explicitly.

The case considered will be a 122.4 Å thick sample of $\langle 110 \rangle$ ZnS (16 repeat distances along

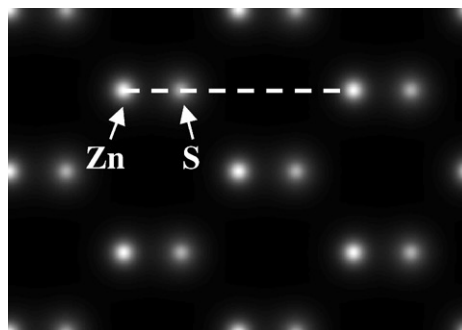


Fig. 4. The projected potential for $\langle 110 \rangle$ ZnS. The locations of columns of Zn and S are shown, as is the line scan used in Fig. 5.

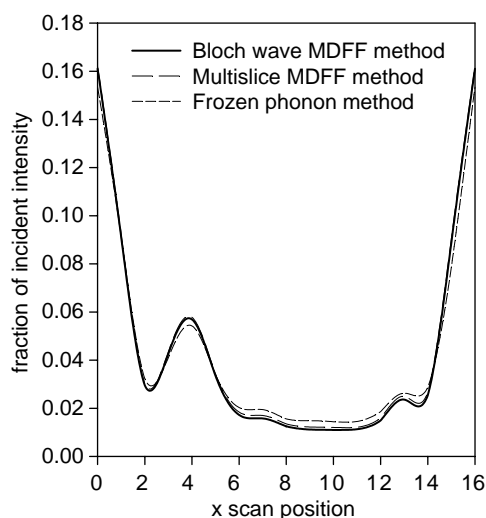


Fig. 5. ADF STEM image contrast along the line scan (shown in Fig. 4) for the case of 200 keV electrons incident along the $\langle 110 \rangle$ zone axis of ZnS. The spherical aberration is $C_s = 0.05$ mm, with the corresponding Scherzer defocus of $\Delta f = 129.3$ Å and optimal cutoff of 0.90 Å $^{-1}$. The annular detector is taken to span 40–80 mrad. It is seen that the two MDFF formalisms, theoretically equivalent but possessing distinct encodings, do indeed give virtually identical results. It is seen that the FPh model is in excellent agreement with the results of the MDFF models. For this case, the discrepancies between these single and double channelling models are small.

the propagation direction). The incident energy is taken as 200 keV. The spherical aberration coefficient is assumed to be $C_s = 0.05$ mm, with the corresponding Scherzer defocus $\Delta f = 129.3$ Å and optimal cutoff of 0.90 Å $^{-1}$. The annular detector is taken to span the range 40–80 mrad. Fig. 5 shows

the line scans simulated for these parameters in the Bloch wave MDFF model (solid line), the multislice MDFF model (long dashed line) and the FPh model (short dashed line). The Bloch wave MDFF model uses 129 beams in each of the sub-matrices of the block diagonalised structure matrix and an 8×8 supercell. The multislice MDFF model used a 512×512 grid inside which the unit cell used was tiled 8×6 times. For the FPh model, adequate convergence required a 1024×1024 grid (the FPh model being more susceptible to errors in the high frequency range) inside which the unit cell used was also tiled 8×6 times. In the FPh case the unit cell was sliced as per a higher order Laue zone (HOLZ) simulation as is the usual practice, although HOLZ effects are believed to make a small contribution to ADF imaging [18], a notion borne out by our calculations.

It is readily seen from Fig. 5 that the agreement between the two distinct codings of the MDFF model is excellent. The comparison of the results of the MDFF model with the FPh model is also very favourable. This implies that the contribution to the image from coherently scattered electrons and the effect of double channelling of thermally scattered electrons are small for the example considered here.

The theoretical basis of the FPh model, inherently taking double channelling into account, is superior to that of the MDFF model (for ADF) and as such the accuracy of the FPh model will naturally be preferred in many cases. However there is another concern which should not be wholly neglected in choosing between the three methods discussed and that is computation time.

Let us first neglect the FPh model and consider only the comparison between the two MDFF models. For the case of perfect crystals, the block diagonalisation of the \mathcal{A} -matrix makes the Bloch wave method very efficient for the calculation of STEM images.¹ For such cases the Bloch wave

method is to be preferred. However, consider now the simulation of diffraction through imperfect (defect) structures. One standard method of treating such structures is to use supercells (the method of periodic continuation [34,35]) and so is naturally suited to the requirements of STEM calculations. The multislice MDFF coding is equally amenable to this case as to the periodic case, however, as regards the Bloch wave implementation, the block diagonalisation property is lost. Thus for such cases it is often the multislice method that is to be preferred. A further consideration is that the multislice calculation time scales linearly with thickness whilst the Bloch wave calculation time is independent of the value of the thickness.

We have neglected the FPh model in the above discussion because the MDFF model is applicable to any form of incoherent scattering for which the form factors may be calculated. Such examples include EDX analysis and EELS. The FPh model has been primarily restricted to the simulation of ADF images. If we now consider ADF simulations then all three models are viable choices. For a single “run” through the crystal, the FPh model and multislice MDFF model take the same amount of computation time. However in order to adequately sample the phonon configuration space in the Monte Carlo type integration in the FPh model, it becomes necessary to propagate through the crystal many times for each probe point considered. Our calculations have used 20 points in the Monte Carlo integration, Loane et al. [14] give a similar number as adequate. Thus while the FPh model is theoretically preferred, a converged FPh calculation takes around 20 times longer than a multislice MDFF calculation. Accuracy cannot be divorced from the choice of algorithm, however when there is reason to believe that the MDFF model will give adequate results

¹ It should be noted that the conceptualisation of the coupling of reciprocal vectors differing by physical reciprocal lattice vectors, and the decoupling between sets which are not, is a physical effect and thus not particular to the Bloch wave model. A Fourier space encoding of the multislice could equally well be “block diagonalised” by separately propagating the different vector sets. Thus in principle one may, say, perform 8 multislice

(footnote continued)

calculations on 64×64 grids rather than a single calculation on a 512×512 grid. However, it is our experience that the requirements of adequate sampling in the multislice require the “block diagonal” grids to be large and as such the computational saving afforded is smaller than that of the Bloch wave model.

Table 1
Comparison of computation times and scaling behaviour between the models

Model	Bloch wave MDFF	Multislice MDFF	FPh
Calculation time for Fig. 5	70 s	420 s	12×10^3 s
Scaling with point number	Non-linear	Linear	Linear
Scaling with thickness	None	Linear	Linear
Scaling with “run” number	—	—	Linear

A dash denotes that a category is not applicable to that particular algorithm.

(as in our test case), its relative computational simplicity makes it extremely competitive.

Table 1 shows the computation times for the case shown in Fig. 5, with the exception that the FPh model times refer to a 512×512 grid for fair comparison with the multislice MDFF model (which computationally corresponds to a small sacrifice in accuracy of the FPh model). It also shows how the different algorithms scale with the number of pixels used in the scan (or image), with the sample thickness, and, for the FPh case, with the number of times one traverses the sample in the Monte Carlo style integration, the “run” number. Note that the Bloch wave method is not precisely linear with pixel number since the eigenvalue problem must be performed in entirety regardless of the number of points scanned. Once performed, the remaining time in the Bloch wave calculation scales linearly with number of points. Note that the Bloch wave computation time is independent of crystal thickness. The difference in time between the multislice MDFF model and the FPh model is primarily due to the requirement in the latter of propagating multiple times through the crystal for each point—20 times in our simulation.

We stress again that accuracy is always the primary consideration. However, in cases where all models are of similar validity, the computation times and scaling behaviour in Table 1 should be considered carefully in the selection of the algorithm to be used.

8. Summary and conclusions

In the Bloch wave formulation of the previous paper [1] the boundary conditions for STEM were applied by requiring continuity of the entire wave

function. It has been shown here that the resultant \mathcal{A} -matrix, which embodies the solution of the Schrödinger equation, may be block diagonalised in the case of perfect crystals. This leads to a more efficient implementation of that algorithm, but more importantly gives considerable insight into the physics of the coupling between the probe and the electron wave function within the crystal. It has been seen that plane wave components in the incident probe which differ by what have been called physical reciprocal lattice vectors can profitably be treated together, while those which do not differ by such vectors do not interact within the crystal.

This conceptualisation led to a proof of the equivalence with the prevalent method for the boundary conditions (the coherent superposition of phase-linked plane waves), an increase in the efficiency of the cross-section calculation and simple proofs of some well-known properties of STEM images. Thus the authors consider this approach to have, in addition to computational convenience, much pedagogical merit.

The numerical agreement between the Bloch wave and multislice methods for calculation of incoherent lattice contrast in the MDFF method was presented. The excellent agreement obtained allows this technique to be applied in a variety of situations where the particular computational technique may be selected based on the problem in question. For fairly simple structures, where the dependence on parameters such as thickness, spherical aberration and defocus are of interest, the Bloch wave method is most apt; it allows ready simulation of all requisite images while only solving once for the wave function. Conversely, for more complex structures, particularly structures with defects, the multislice method may be preferred. In such cases it is computationally

simpler; the Bloch wave method becomes cumbersome when block diagonalisation is no longer possible and the number of beams involved is large.

The FPh model, which is theoretically preferable but computationally demanding, was also compared with the MDFF method, with the conclusion that the discrepancy between these models is in some cases very small. As such, the speed provided by the latter makes it competitive.

Acknowledgements

L.J.A. thanks Dr A.E.C. Spargo for helpful discussions and acknowledges financial support from the Australian Research Council. M.P.O. acknowledges financial support from the Australian Research Council. C.J.R. acknowledges a visit to Fujitsu Laboratories in Atsugi, Japan, under the auspices of their Visiting Research Specialist Programme, which stimulated part of this work. The authors thank Dr P. Rez for informative and stimulating correspondence.

Appendix A. The small aperture limit for coherent contrast

It was proven in Section 6 that incoherent STEM images contained no contrast if the aperture was too small to admit two beams which differed by a physical reciprocal lattice vector. A similar line of reasoning serves to prove the more common statement that there is no coherent image contrast as a function of probe position if the CBED disks do not overlap [20]. The criterion of no overlap is precisely the criterion that no two beams in the aperture differ by a physical reciprocal lattice vector.

The coherent amplitude $A_{\mathbf{g}}$ scattered to a point \mathbf{g} in the far field (diffraction pattern) is obtained by Fourier transformation of the exit surface wave function, i.e.

$$A_{\mathbf{g}} = \sum_i C_{\mathbf{g}}^i \exp(2\pi i \lambda^i t) \sum_{\mathbf{h}} C_{\mathbf{h}}^{i*} \times \exp(-2\pi i \mathbf{h} \cdot \mathbf{R}) T(\mathbf{h}), \quad (\text{A.1})$$

where the index \mathbf{h} is used for points which lie within the aperture. A ronchigram [36] is obtained from the intensity distribution as a function of \mathbf{g} and, if a detector is located at the origin and the maximum momentum transfer admitted by the lens, p_{\max} , is sufficiently large [27], a coherent STEM lattice image $|A_0(\mathbf{R})|^2$ may be calculated as a function of probe position \mathbf{R} .

Now, choosing a particular direction $\mathbf{g} = \mathbf{G} + \mathbf{q}_l$ restricts the i values for which the element $C_{\mathbf{g}}^i$ are non-zero to a subset $C_{\mathbf{G}}^k(\mathbf{q}_l)$. So

$$A_{\mathbf{G}+\mathbf{q}_l} = \sum_k C_{\mathbf{G}}^k(\mathbf{q}_l) \exp(2\pi i \lambda^k t) \times \sum_{\mathbf{h}} C_{\mathbf{h}}^{k*} \exp(-2\pi i \mathbf{h} \cdot \mathbf{R}) T(\mathbf{h}). \quad (\text{A.2})$$

This in turn restricts the possible values of \mathbf{h} for which $C_{\mathbf{h}}^{k*}$ is non-zero, specifically to $\mathbf{H} + \mathbf{q}_l$. Thus

$$A_{\mathbf{G}+\mathbf{q}_l} = \sum_k C_{\mathbf{G}}^k(\mathbf{q}_l) \exp(2\pi i \lambda^k t) \sum_{\mathbf{H}} C_{\mathbf{H}}^{k*}(\mathbf{q}_l) \times \exp[-2\pi i (\mathbf{H} + \mathbf{q}_l) \cdot \mathbf{R}] T(\mathbf{H} + \mathbf{q}_l). \quad (\text{A.3})$$

Using Eq. (44), which expresses that the aperture is centred about the origin in reciprocal space (i.e. the wave vector \mathbf{k} is normal to the surface; an unnecessary but typical condition) we obtain

$$A_{\mathbf{G}+\mathbf{q}_l} = \sum_k C_{\mathbf{G}}^k(\mathbf{q}_l) \exp(2\pi i \lambda^k t) C_0^{k*}(\mathbf{q}_l) \times \exp(-2\pi i \mathbf{q}_l \cdot \mathbf{R}) T(\mathbf{q}_l). \quad (\text{A.4})$$

The exponential term in \mathbf{R} is independent of k and so may be brought out of the sum as a phasing term. As a result, the intensity of the $\mathbf{g} = \mathbf{G} + \mathbf{q}_l$ diffraction beam, given by $|A_{\mathbf{G}+\mathbf{q}_l}|^2$, is independent of \mathbf{R} ; there is no contrast in such an image. This completes the proof.

References

- [1] L.J. Allen, S.D. Findlay, M.P. Oxley, C.J. Rossouw, preceding article in this issue, Ultramicroscopy 96 (2003).
- [2] R.F. Loane, E.J. Kirkland, J. Silcox, Acta Crystallogr. A 44 (1988) 912–927.
- [3] S.C. Anderson, C.R. Birkeland, G.R. Anstis, D.J.H. Cockayne, Ultramicroscopy 69 (1997) 83–103.
- [4] S. Hillyard, R.F. Loane, J. Silcox, Ultramicroscopy 49 (1993) 14–25.

- [5] S.J. Pennycook, D.K. Jesson, *Ultramicroscopy* 37 (1990) 14–38.
- [6] P.D. Nellist, S.J. Pennycook, *Ultramicroscopy* 78 (1999) 111–124.
- [7] P.D. Nellist, S.J. Pennycook, *Adv. Imaging Electron Phys.* 113 (2000) 147–203.
- [8] T. Yamazaki, K. Watanabe, A. Recnik, M. Ceh, M. Kawasaki, M. Shiojiri, *J. Electron Microsc.* 49 (2000) 753–759.
- [9] T. Yamazaki, K. Watanabe, Y. Kikuchi, M. Kawasaki, I. Hashimoto, M. Shiojiri, *Phys. Rev. B* 61 (2000) 13833–13839.
- [10] K. Watanabe, T. Yamazaki, Y. Kikuchi, Y. Kotaka, M. Kawasaki, I. Hashimoto, M. Shiojiri, *Phys. Rev. B* 63 (2000) 085316 (5 pp.).
- [11] P. Rez, private communication, 2001.
- [12] L.J. Allen, T.W. Josefsson, *Phys. Rev. B* 53 (1996) 11285–11287.
- [13] R.F. Loane, X. Peirong, J. Silcox, *Acta Crystallogr. A* 47 (1991) 267–278.
- [14] R.F. Loane, X. Peirong, J. Silcox, *Ultramicroscopy* 40 (1992) 121–138.
- [15] C.J. Humphreys, *Rep. Prog. Phys.* 42 (1979) 1825–1887.
- [16] L.J. Allen, T.W. Josefsson, H. Leeb, *Acta Crystallogr. A* 54 (1998) 388–398.
- [17] L.J. Allen, H.M.L. Faulkner, H. Leeb, *Acta. Crystallogr. A* 56 (2000) 119–126.
- [18] A. Amali, P. Rez, *Microsc. Microanal.* 3 (1997) 28–46.
- [19] K. Watanabe, T. Yamazaki, I. Hashimoto, M. Shiojiri, *Phys. Rev. B* 64 (2001) 115432 (5 pp.).
- [20] P.G. Self, O’Keefe, in: P.R. Buseck, J.M. Cowley, L. Eyring (Eds.), *High-Resolution Transmission Electron Microscopy*, Oxford University Press, Oxford, 1988, pp. 244–307.
- [21] G. Kästner, *Many Beam Electron Diffraction Related to Electron Microscope Diffraction Contrast* Akademie Verlag, Berlin, 1993, pp. 9–19.
- [22] J.M. Cowley, *Appl. Phys. Lett.* 15 (1969) 58–59.
- [23] Z.L. Wang, *Elastic and Inelastic Scattering in Electron Diffraction and Imaging*, Plenum Press, New York, London, 1995, pp. 241–246.
- [24] E.J. Kirkland, *Advanced Computing in Electron Microscopy*, Plenum Press, New York, London, 1998, pp. 14–16.
- [25] A.P. Pogany, P.S. Turner, *Acta Crystallogr. A* 24 (1968) 103–109.
- [26] W.H. Press, S.A. Teukolsky, W.T. Vetterling, B.P. Flannery, *Numerical Recipes in FORTRAN*, 2nd Edition, Cambridge University Press, Cambridge, 1992, pp. 449–489.
- [27] J.C.H. Spence, J.M. Cowley, *Optik* 50 (1978) 129–142.
- [28] K. Ishizuka, *J. Electron Microsc.* 50 (2001) 291–305.
- [29] K. Ishizuka, *Ultramicroscopy* 90 (2002) 71–83.
- [30] L.J. Allen, C.J. Rossouw, *Phys. Rev. B* 39 (1989) 8313–8321.
- [31] C.J. Rossouw, *Ultramicroscopy* 58 (1995) 211–222.
- [32] L.J. Allen, T.W. Josefsson, *Phys. Rev. B* 52 (1995) 3184–3198.
- [33] C.J. Rossouw, C.T. Forwood, M.A. Gibson, P.R. Miller, *Micron* 28 (1997) 125–137.
- [34] P.M. Fields, J.M. Cowley, *Acta Crystallogr. A* 34 (1978) 103–112.
- [35] J.M. Cowley, P.M. Fields, *Acta Crystallogr. A* 35 (1979) 28–37.
- [36] J.C.H. Spence, *Mater. Sci. Eng.* 26 (1999) 1–49.